The Astrophysical Journal, 874:138 (9pp), 2019 April 1 https://doi.org/10.3847/1538-4357/ab09ef

Detecting the Sagittarius Stream with LAMOST DR4 M Giants and *Gaia* DR2

Jing Li[1,2]
(LAMOST FELLOW),
and
Chao Liu[3], Xiangxiang Xue[3], Jing Zhong[2], Jake Weiss[4], Jeffrey L. Carlin[5], and Hao Tian[3]
(LAMOST FELLOW)

[1] Physics and Space Science College,China West Normal University, 1 ShiDa Road, Nanchong 637002, People's Republic of China; lijing@shao.ac.cn
[2] SHAO, Chinese Academy of Sciences, Nandan Road, Shanghai 200030, People's Republic of China
[3] Key Laboratory of Optical Astronomy, National Astronomical Observatories, Chinese Academy of Sciences, Datun Road 20A, Beijing 100012, People's Republic of China
[4] Department of Physics, Applied Physics and Astronomy, Rensselaer Polytechnic Institute, 110 Eighth Street, Troy, NY 12180, USA
[5] LSST, 950 North Cherry Avenue, Tucson, AZ 85719, USA
Received 2018 June 1; revised 2019 February 20; accepted 2019 February 21; published 2019 April 1

Abstract

We use LAMOST DR4 M giants combined with *Gaia* DR2 proper motions and ALLWISE photometry to obtain an extremely pure sample of Sagittarius (Sgr) stream stars. Using TiO5 and CaH spectral indices as indicators, we selected a large sample of M-giant stars from M-dwarf stars in LAMOST DR4 spectra. Considering the position, distance, proper motion, and angular momentum distribution, we obtained 164 pure Sgr stream stars. We find that the trailing arm has higher energy than the leading arm in the same angular momentum. The trailing arm we detected extends to a heliocentric distance of ∼130 kpc at $\tilde{\Lambda}_{\odot} \sim 170°$, which is consistent with the feature found in RR Lyrae in Sesar et al. Both of these detections of Sgr, in M-giants and in RR Lyrae, imply that the Sgr stream may contain multiple stellar populations with a broad metallicity range.

Key words: galaxies: individual (Sagittarius dSph) – Galaxy: halo – Galaxy: structure – stars: abundances – stars: distances – stars: late-type

Supporting material: FITS file

1. Introduction

Dwarf galaxies that come too close to the larger host galaxy suffer tidal disruption; the gravitational force between one side of the galaxy and the other serves to rip the stars from the dwarf galaxy. This produces stellar tidal streams, which have been found in the stellar halo of the Milky Way (Newberg & Carlin 2016).

The Sagittarius (Sgr) stream is the most prominent and extensive coherent stellar tidal stream in the Milky Way. Over the last 20 years, it has been shown that the Sgr streams wrap around the entire Milky Way twice (Ibata et al. 1994; Newberg et al. 2002; Majewski et al. 2003; Belokurov et al. 2006, 2014; Koposov et al. 2012, 2014; Li et al. 2016). Previously, a wide variety of stellar types have been used to trace Sgr tidal debris. For example, the main-sequence turn-off stars, blue horizontal branch (BHB) stars, Red giants, RR Lyrae, and M giants. Recent studies closed the controversy over the potential detection of the apo-center of the trailing tail of the Sagittarius stream (Belokurov et al. 2014; Koposov et al. 2015). They demonstrated that at Sgr longitudes $\tilde{\Lambda}_{\odot}$[6] close to the apo-center, the line-of-sight velocity of the trailing tail starts to deviate from the track of the Law & Majewski (2010; L&M) model, and redefined the maximal extent for trailing tail stars to a Galactic distance of $R = 102.5$ kpc.

Recently, Sesar et al. (2017b) reported the detection of spatially distinct stellar density features near the apocenters of the Sgr stream's main leading and trailing arm, and found a "spur" extending to 130 kpc at the apo-center of the trailing arm using Pan-STARRS1 Type ab RR Lyrae (RRab) stars. The objects in their sample are expected to be true RRab stars with 90% purity. The distance modulus uncertainties are $\sigma_{\rm DM} = 0.06(\rm rnd) \pm 0.03(\rm sys)$ mag, corresponding to a distance uncertainty of 3% (Sesar et al. 2017a).

Studies of the metallicity distribution of metal-rich red giants stars show an average metallicity for Sgr stream stars that is lower than the average metallicity for stars in the Sgr core. It has also been shown that stars in the trailing and leading arms have metallicity differences (Carlin et al. 2018). Chou et al. (2007) studied the variation of the metallicity distribution function along the Sgr stream, showing the leading arm has a significant metallicity gradient, providing evidence that there can be significant chemical differences between current dwarf spheroidal satellites and the bulk of the stars they have contributed to the halo. These differences exist due to preferential stripping of older stars from the core.

In this paper, we map the 6D phase space of M giants from the Sgr stream in LAMOST using LAMOST radial velocities combined with *Gaia* DR2 (Gaia Collaboration et al. 2018) proper motions. The paper is organized as follows. In Section 2, we describe how we select M giants and how we determine the distance, metallicity, velocity, energy, and angular momentum for each M giant. In Section 3, we describe the various features of the Sgr stream. In Section 4, we present a brief discussion and conclusion.

[6] $(\tilde{B}_{\odot}, \tilde{\Lambda}_{\odot})$ in latitude and longitude in the Sgr stream coordinate system. The Sgr orbit plane is defined following the equations in the Appendix of Belokurov et al. (2014), which are related to the Majewski et al. (2003) system through $\tilde{\Lambda}_{\odot} = 360 - \Lambda_{\odot}$ and $\tilde{B}_{\odot} = -B_{\odot}$.

2. Data

2.1. M-giant Sample

The LAMOST Telescope is a 4 m Schmidt telescope at the Xinglong Observing Station; this National Key Scientific facility was built by the Chinese Academy of Sciences (Cui et al. 2012; Zhao et al. 2012). The main goal of the LAMOST spectroscopic survey is to provide A-, F-, G-, K-, and M-type stars to improve our understanding of the structure of the Milky Way (Deng et al. 2012). Although the standard data processing pipeline provides an accurate estimation of the stellar atmospheric parameters for the AFGK-type stars, it does not reliably identify M-type stars (Luo et al. 2015). Zhong et al. (2015) selected a large sample of M-giant and M-dwarf stars from the LAMOST DR1 catalog using a template fitting method. Using this method and selecting only spectra with a signal-to-noise $(S/N) > 5$, we find over 490,000 spectra that show the characteristic molecular titanium oxide(TiO), vanadium oxide (VO), and calcium hydride(CaH) features typical of M-type stars in LAMOST DR4 data. The TiO and CaH spectral indices were defined by Reid et al. (1995) and Lépine et al. (2007), and the distribution of the spectral indices is a good indicator for separating M-dwarf stars with different metallicities (Gizis 1997; Lépine et al. 2003, 2007, 2013; Mann et al. 2012). Zhong et al. (2015) showed that M giants generally have weaker CaH molecular bands for a given range of TiO5 values. This spectral index distribution of M-type stars can be used to separate giants from dwarfs with little contamination. Following the method in Zhong et al. (2015), we selected 33,000 M giants from the LAMOST DR4 sample.

Next, we calculated the heliocentric radial velocity (RV) of all M-giant stars by using a cross-correlation method with a template spectrum in a zero-velocity rest frame; the same method is used in Zhong et al. (2015). This procedure was repeated until the measured RV for each corrected training spectrum was less than $\pm 5\,\mathrm{km\,s^{-1}}$ from the published value.

Finally, using the TiO and CaH spectral indices we identified 33,000 M-giant stars from the LAMOST DR4 sample. Then we cross-matched this sample to the ALLWISE Source Catalog (Wright et al. 2010) in NASA/IPAC Infrared Science Archive, using a search radius of 3″. More than 99% of the M giants from LAMOST DR4 had search radii less than 3″ in the ALLWISE Source Catalog, and we obtained five photometric bands for these stars (J, H, K, $W1$, and $W2$). The details for our selection criteria are the same as those in Section 3.1 of Li et al. (2016). The interstellar reddening is corrected using the same spatial model of the extinction mentioned in Li et al. (2016). We adopt the $E(B-V)$ maps of Schlegel et al. (1998), in combination with $A_r/E(B-V) = 2.285$ from Schlafly & Finkbeiner (2011) and $A_\lambda/A(r)$ from Davenport et al. (2014).

Thanks to the presence of the gravity-sensitive CO bands in *Wide-field Infrared Survey Explorer* (*WISE*) photometry, metal-rich giants stands out from the dwarfs (Meyer et al. 1998; Koposov et al. 2015). We purify our sample by excluding a few contaminating K-giant stars and M-dwarf stars using the photometric selection criteria of the *WISE* color index $(W_1 - W_2)_0$; for more details see Equation (1) of Li et al. (2016). Finally we get 22,999 M-giant stars. We also removed contamination from 894 carbon stars by cross-matching with the latest LAMOST carbon star catalog (Ji et al. 2016; Li et al. 2018).

2.2. Distance

Li et al. (2016) has constructed a new photometric distance relation using a large sample of M giants from the Sagittarius (Sgr), LMC, and SMC structures. The variation in these distance relations (see the parameters in Table 1 of Li et al. 2016) reflects the differing chemical composition of these structures. The distances were computed using the color index $(J-K)_0$ to get the absolute J-band magnitude, M_J, using the relation described in Li et al. (2016). In the ALLWISE Source Catalog, the mean photometric errors for our M giants are $\delta J = \pm 0.238$ mag, $\delta K = \pm 0.029$ mag, $\delta W1 = \pm 0.008$ mag, and $\delta W2 = \pm 0.008$ mag. The J-band magnitude error is much larger in our full M-giant sample than the sample selected by Li et al. (2016) because most LAMOST observed regions are located at lower Galactic latitudes, close to the plane where the extinction uncertainty has a larger effect on the accuracy of J-band magnitude. In this work we only consider the Sgr stream members (Sgr stream member selection is described in Section 3.1), and as such most of the candidates are located at higher galactic latitude. Since we are working at high galactic latitude where the extinction is low, the J-band magnitude error is smaller than the LAMOST average. For Sgr member candidates, the mean $\delta J = 0.0298$ mag, $\delta K = 0.009$ mag, $\delta W1 = 0.004$ mag, and $\delta W2 = 0.003$ mag, and therefore are negligible in our distance uncertainty computation.

In Li et al. (2016), the $(J-K)_0$ color–distance relation for M-giant stars was shown to have some uncertainty due to an absolute magnitude dispersion around their best-fit model. This absolute magnitude dispersion was found to be around 0.36 mag and translates to a distance uncertainty of about 20%. Since we use the same color–distance relation in our work, we also expect to have a distance uncertainty of 20%. Although the distance uncertainty for an individual M giant is relatively large, for structures like the Sgr stream, we should have relatively high precision because the distance relation is calibrated with the Sgr core member stars (Li et al. 2016).

Figure 1 shows the heliocentric-distance and RV distribution for all of our selected M giants. As we can see, the distance of most of the M-giant stars is smaller than 20 kpc, with only 700 stars having distances larger than 20 kpc. For these 700 stars we checked the spectra by eye to ensure they are true M-giant stars. Of these ~700 stars, about 50 were not true M giants, and they were removed from the sample. We only select the stars with distances larger than 20 kpc as candidates for selecting Sgr members.

2.3. Proper Motion and Velocity

Since *Gaia* published its DR2 data consisting of astrometry, photometry, RVs, astrophysical parameters, and the unprecedentedly high accuracy proper motion, we have the chance to determine 6D phase-space information for our catalog of M giants (Gaia Collaboration et al. 2018). We cross-matched our M giants with *Gaia* DR2 data using a cross-match radius of 3″. We found 94% of the stars in our Sgr candidate sample had matching stars in the *Gaia* data. The mean proper motion error in pmra is $0.14\,\mathrm{mas\,yr^{-1}}$ and pmdec is $0.10\,\mathrm{mas\,yr^{-1}}$ with a dispersion in these means of 0.08 and 0.06, respectively.

For each star, we calculated the line-of-sight Galactic standard of rest velocity from the heliocentric RV using the formula:

$$V_{\mathrm{gsr}} = \mathrm{RV} + 10\cos l\cos b + 225.2\sin l\cos b + 7.2\sin b$$

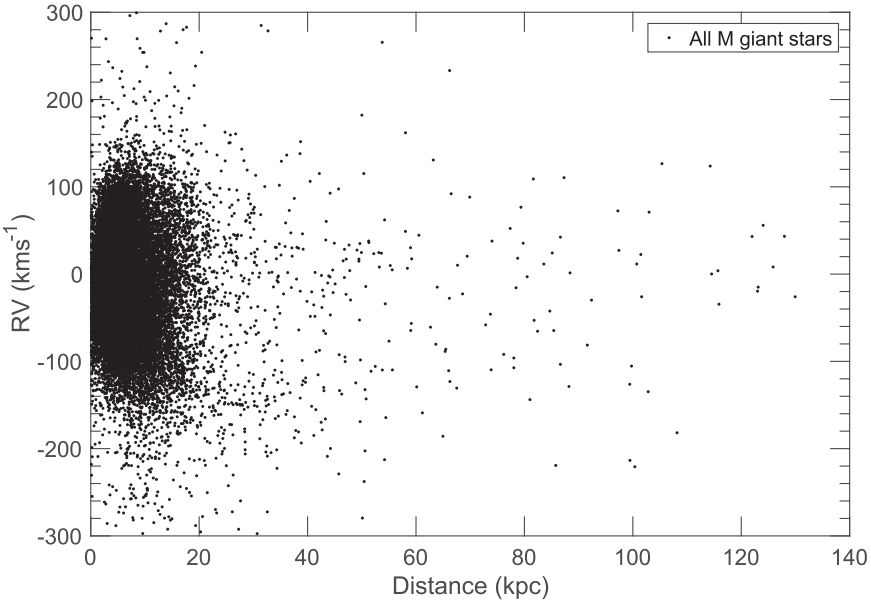

Figure 1. Radial velocity as a function of heliocentric distance for all our M-giant stars selected from the LAMOST DR4 sample. We see that most stars are within 20 kpc. Of these stars, we only select stars with a distance greater than 20 kpc to be Sgr candidate members.

Table 1
The Parameters for Sagittarius Stream Members

	R.A. (deg)	Decl. (deg)	$\tilde{\Lambda}_\odot$ (deg)	$\tilde{B}_\odot$ (deg)	J_0 (mag)	H_0 (mag)	K_0 (mag)	$W1_0$ (mag)	$W2_0$ (mag)	RV (kms^{-1})
1	−184.98	14.71	2.03	268.39	11.25	11.88	11.06	10.84	10.85	10.97
2	−152.44	20.12	−2.73	266.00	4.44	12.04	11.12	10.93	10.85	10.96
	V_{gsr} (kms^{-1})	$D_\odot$ (kpc)	[Fe/H] (dex)	S/N ⋯	X_{GC} (kpc)	Y_{GC} (kpc)	Z_{GC} (kpc)	V_x (kms^{-1})	V_y (kms^{-1})	V_z (kms^{-1})
1	−106.08	23.45	−1.62	14.75	15.14	9.17	−20.46	−291.55	−2.65	14.75
2	−100.29	28.99	−0.83	24.28	17.82	7.97	−26.19	−327.34	−47.52	−27.84
	pmRA (masy^{-1})	pmRA$_{error}$ (masy^{-1})	pmDec (masy^{-1})	pmDec$_{error}$ (masy^{-1})	E (km^{2}s^{-2})	L (km^{2}s^{-2})	L_x (km^{2}s^{-2})	L_y (km^{2}s^{-2})	L_z (km^{2}s^{-2})	
1	−0.86	0.07	−2.79	0.04	−42303.85	6318.78	81.06	5743.09	2633.87	
2	−0.625	0.08	−2.87	0.05	−23328.86	9355.16	−1466.55	9069.79	1762.69	

(This table is available in its entirety in FITS format.)

kms^{-1}. This formula removes the contributions from the 220 kms^{-1} (Dehnen 2000) rotation velocity at the solar circle as well as the solar peculiar motion (relative to the local standard of rest) of $(U, V, W)_0 = (10.0, 5.2, 7.2)$ kms^{-1} (Dehnen & Binney 1998).

To determine the energy and angular momenta of the stars in our sample, we first convert from proper motion and RV to Cartesian velocity (Johnson & Soderblom 1987). The *XYZ* coordinates we use are left-handed, where the *X*-axis is positive toward the Sun and the *Y*-axis is positive in the the direction of Galactic rotation. We also propagate the errors in distance, RV, and proper motion into the errors in our Cartesian velocities using a Monte Carlo method.

2.4. The Energy and Angular Momentum

To calculate the energy and angular momentum for each of our M giants, we assume that the Galactic potential is represented by three components: a spherical bulge, an exponential disk, and an NFW dark matter halo (Navarro et al. 1996). Based on the Galactocentric (X, Y, Z, V_x, V_y, V_z) and potential $\Phi_{tot}(X, Y, Z)$, the four integrals of motion $(E, \boldsymbol{L})$ can be calculated as follows:

$$\begin{aligned} E &= \frac{1}{2}(V_x^2 + V_y^2 + V_z^2) + \Phi_{tot}(\sqrt{x^2 + y^2 + z^2}) \\ L_x &= YV_z - ZV_y \\ L_y &= ZV_x - XV_z \\ L_z &= XV_y - YV_x \\ L &= \sqrt{L_x^2 + L_y^2 + L_z^2}. \end{aligned} \quad (1)$$

Figure 4 shows the orbit distribution of the Sgr stream in the *XYZ* plane. In the *XZ* plane, we can see a clear stream orbit trend.

2.5. Metallicity

Li et al. (2016) shows that the metallicities of M giants have a strong correlation with $(W1 - W2)$ and can be fit with the

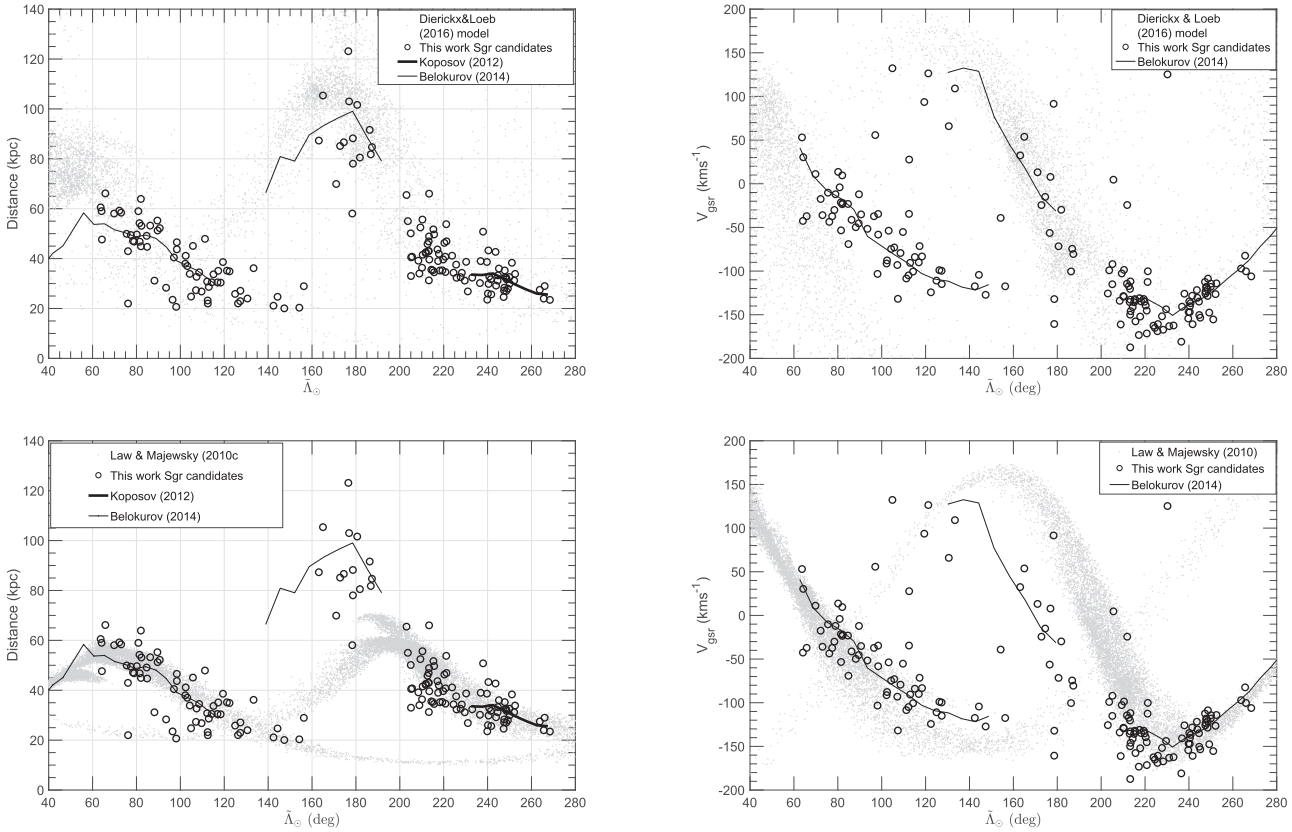

Figure 2. Heliocentric-distance and velocity measurements along the Sgr stream compared to simulations. The top panels overplot our M-giant data (black open circles) on the Dierickx & Loeb (2017) *N*-body model's distribution (gray dots), Belokurov et al. (2014) stream measurements (thin black line), and Koposov et al. (2012) stream measurements (thick black line). The bottom panels are similar, but instead use the L&M *N*-body model's distribution (again as gray points).

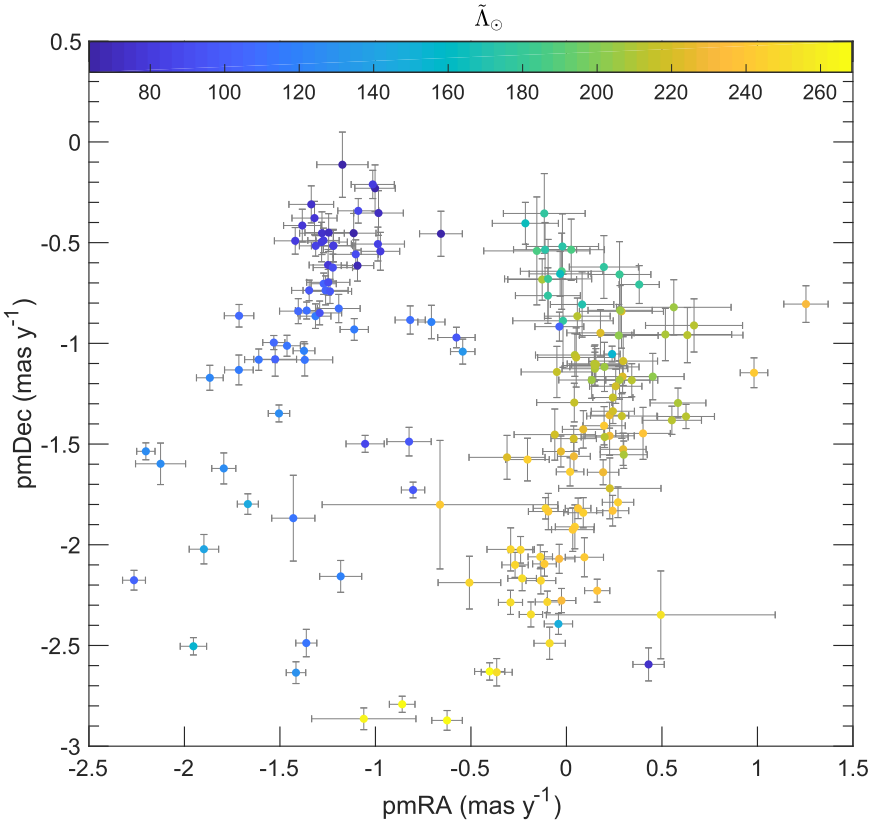

Figure 3. Proper motion distribution of all Sgr stream members. The colors indicate the $\tilde{\Lambda}_{\odot}$ ranges. This figure shows continual proper motion distribution for Sgr leading and trailing members. Most stars have very small proper motion errors.

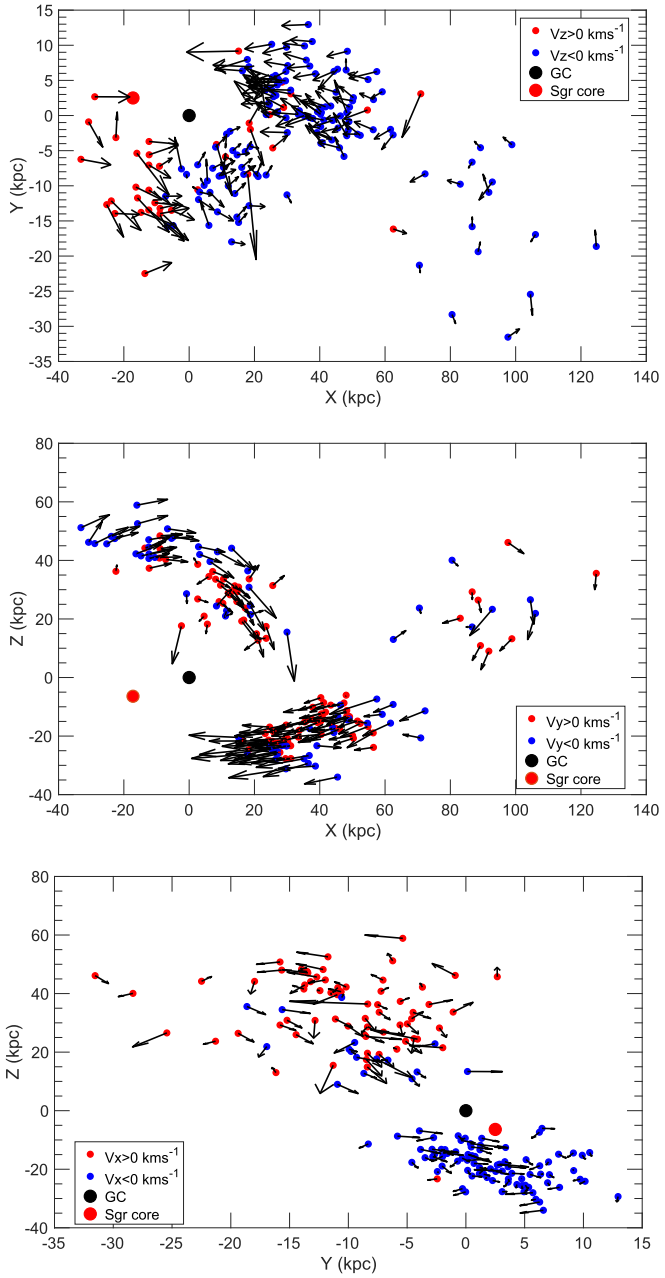

Figure 4. Spatial distribution of the candidate members of the Sgr stream. The arrows show the 3D velocity distribution for Sgr stars in *XYZ* coordinate (left-handed). The red dot marks the location of the Sgr dwarf galaxy (Sgr core). The Galactic center is marked with "GC" and a black dot. The panels show the projection of Sgr stream in (*X, Y*), (*X, Z*), and (*Y, Z*) planes. These figures directly show the orbit distribution of the Sgr stream in the *XYZ* plane.

linear relation: $[\mathrm{M/H}]_{\mathrm{phot}} = -13.2 \times (W1 - W2)_0 - 2.28$ dex, with an uncertainty of 0.35 dex. Clearly $(W1 - W2)_0$ is an acceptable proxy for [M/H]. So using this relation we calculate photometric [M/H] for each M-giant star.

We tried recalibrating our color–metallicity relation using data from APOGEE DR13 (Holtzman et al. 2018). The linear relationship we fit to the APOGEE data was similar to the result Li et al. (2016) found using APOGEE DR12.

For all of our M-giant stars, we now have heliocentric RV, proper motion, S/N determined from the spectrum, distance, and metallicity determined from photometry.

3. Candidate Members of the Sagittarius Stream

3.1. Sgr Candidate Selection

To select candidate members of the Sgr stream from the LAMOST M-giant stars, we first did a broad cut on the total M-giant sample using the selection criteria: $-15° < \tilde{B}_{\odot} < 15°$, $D_{\mathrm{helio}} > 20$ kpc, and S/N > 5. This selection gives a large population of Sgr candidate members that are in the correct region of the sky, and have good enough spectra to determine if they are M giants. Through the distance and velocity distribution, we can easily separate the Sgr stream member from the disk component. We remove stars that are more than 20 kpc from the Sgr orbit in distance and 50 kms^{-1} from the Sgr orbital velocity. Then with these selected stars, we also remove stars that are outside the 2σ distribution in L_x, L_y, and L_z angular momentum distribution. Our final Sgr sample contains a total of 164 candidates, which we are very confident belong to the Sgr stream. We list these stars in Table 1.

Figure 2 shows the distance and V_{gsr} distribution of the pure Sgr stream candidates. The left panels show the distance distribution of the Sgr stream, and the right panels show the velocity distribution of the Sgr stream. In the upper panels, we compare our stars with the Dierickx & Loeb (2017) *N*-body model, and in the lower panels, we compare our stars with the Law & Majewski (2010) *N*-body model. From the figure we can see the leading arm covers a large $\tilde{\Lambda}_{\odot}$ range of 60°–160°, and the trailing arm covers a range of 160°–270°. From the left panel we find many stars extended to the anti-center region and that these stars have a distance of about 100 kpc. Sesar et al. (2017b) find a "spur" structure with RR Lyrae stars that is consistent with the distance to our M-giant detection. Unfortunately, our Sgr sample does not trace the turning back branch feature 1 for the trailing arm from Sesar et al. (2017b).

3.2. Comparison with Models

While we compared our results to many *N*-body models (Law & Majewski 2010; Peñarrubia et al. 2010; Dierickx & Loeb 2017), we limit our discussion to the two that were most consistent with our data; the model from Dierickx & Loeb (2017) and the model from Law & Majewski (2010). L&M model is the first numerical model of the Sgr–Milky Way system that is capable of simultaneously satisfying the majority of major constraints on the angular positions, distances, and radial velocities of the dynamically young tidal debris streams (Law & Majewski 2010). Model from Dierickx & Loeb (2017) is the first to accurately reproduce existing data on the 3D positions and radial velocities of the debris detected 100 kpc away in the MW halo. From the upper panel of Figure 2 we can see the Dierickx & Loeb (2017) model matches the observed data well in distance versus $\tilde{\Lambda}_{\odot}$. We have one star consistent with the "spur" structure in trailing arm apo-center. The velocity distribution in our observed data does not match the model as well as the distance distribution. We can see that the trailing arm velocity matches well, but the leading tail velocity is significantly undervalued compared to our data.

The L&M model was created to reproduce the distance and position of the 2MASS Sgr M giants. In the lower panel of Figure 2, we can see that our M-giant candidates match the distance and velocity of the L&M model's leading and trailing arms well, but they are inconsistent toward the apo-center of the trailing arm ($\tilde{\Lambda}_{\odot} \sim 180°$) both the distance and velocity

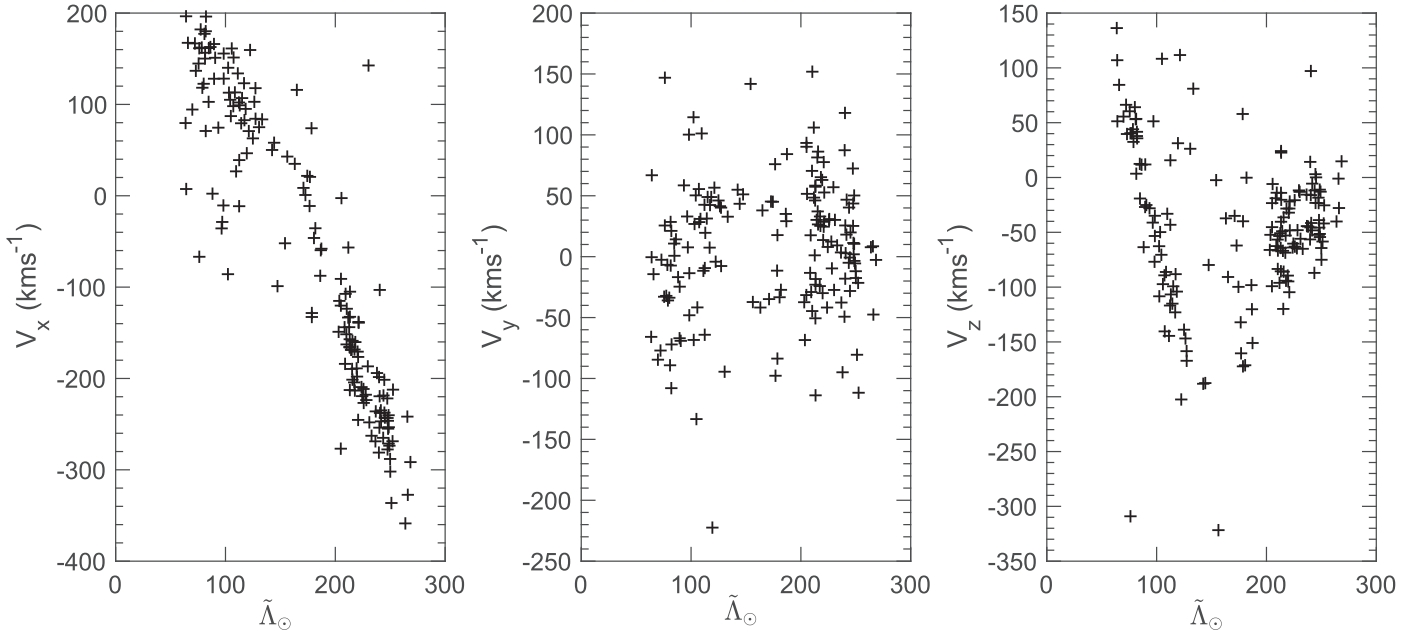

Figure 5. 3D distribution of the Sgr stream. From left to right, the panels show V_x, V_y, and V_z components of the velocity along the $\tilde{\Lambda}_\odot$.

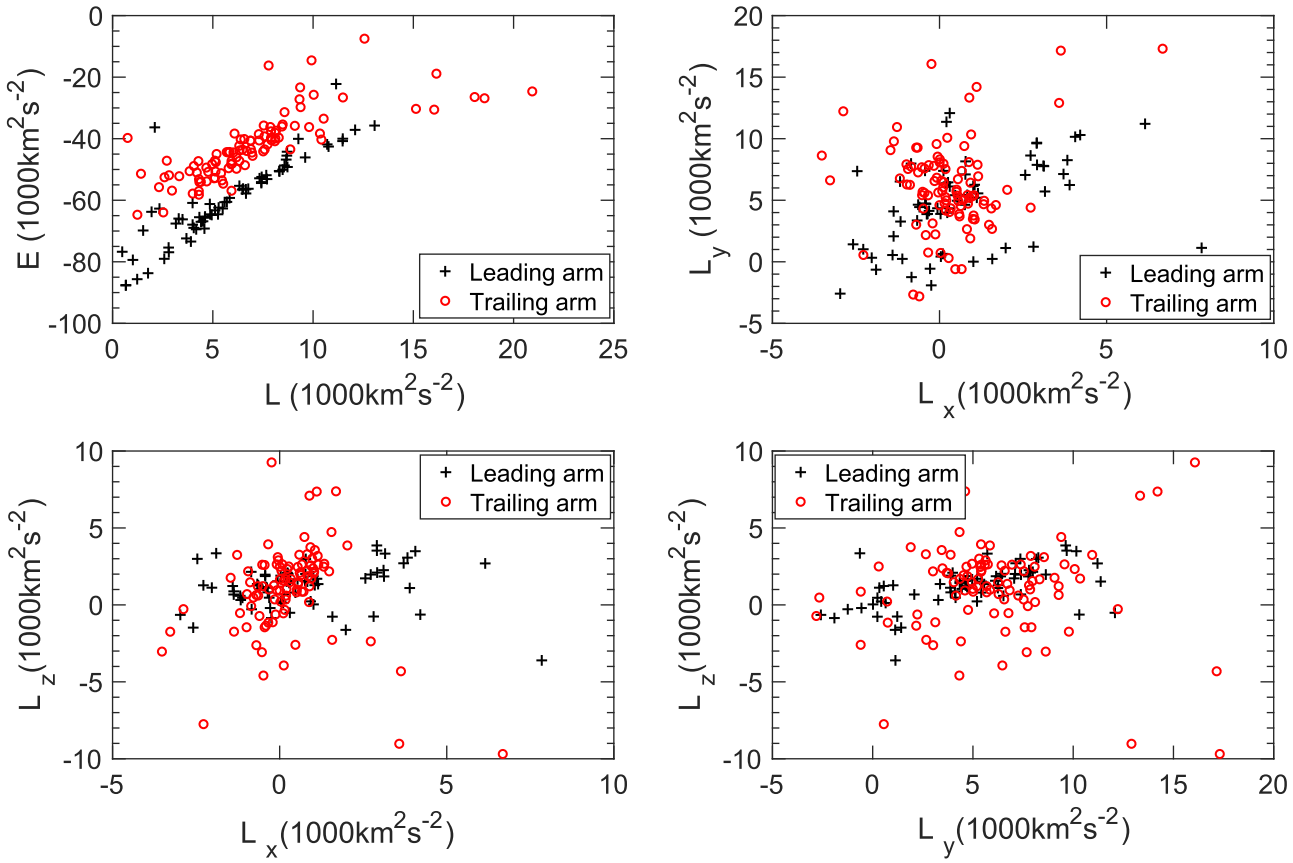

Figure 6. Distribution of the Sgr stream candidates in angular momentum space. The upper left panel shows distribution in energy (E) vs. total angular momentum (L). The rest of the panels show distribution in angular momentum (L_x vs. L_y), (L_x vs. L_z), and (L_y vs. L_z), respectively.

distribution. The apo-centric distance of our M giants in the trailing arm extend to 120 kpc.

From the above discussion, we can see that none of the models can perfectly match with observation. For L&M's *N*-body model, which has no disk rotation and the key element in the success of this model is the introduction of a nonaxisymmetric component to the Galactic gravitational potential, the distance for the trailing is obviously a lower estimation, and the velocity for the trailing tail that crosses to the north hemisphere is significantly shifted. Another model is derived by Dierickx & Loeb (2017), which combined analytic modeling and *N*-body simulations. This model can be well

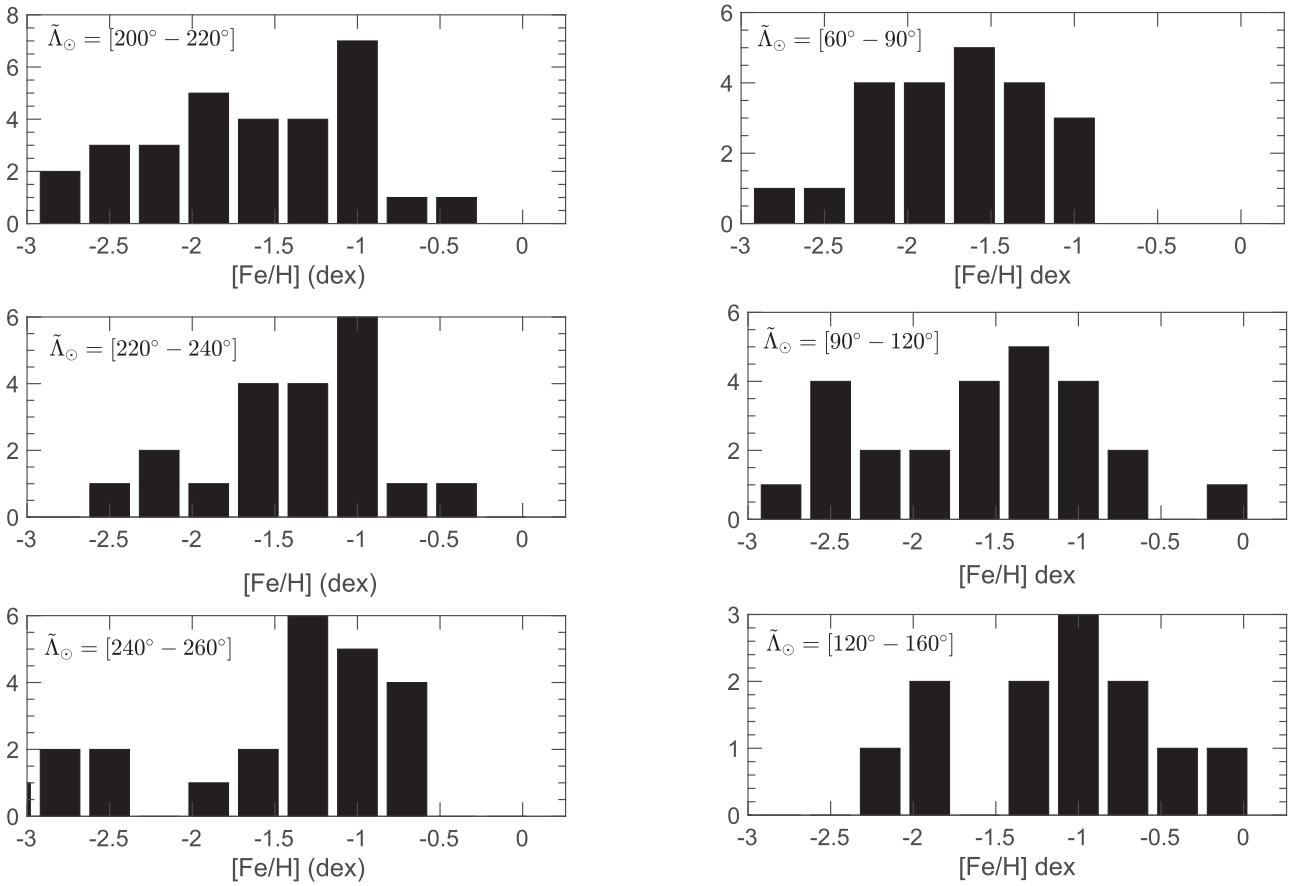

Figure 7. [Fe/H] distribution of trailing/leading tail in different $\tilde{\Lambda}_\odot$ ranges. The left panel shows the trailing arm and the right panel shows the leading arm of the 164 Sgr M giants. We can see that both the leading and trailing arms have a broad metallicity distribution.

compared to the observation in the distance distribution, even the "spur" structure out to the 100 kpc detected by RRly and our M giants. We actually also compared our data to the *N*-body model originally with a late-type, rotating disk galaxy (Peñarrubia et al. 2010), but both the velocity and the distance are not consistent.

3.3. The Phase-space Distribution of the Sgr Stream

With distances estimated from photometry (to ∼20%), radial velocities from spectroscopy (to ∼7 kms^{-1}), and proper motions uncertainty (to ∼0.13 masy^{-1} and ∼0.09 masy^{-1} in R.A. and decl. derictions separately) from *Gaia* DR2, we are able to analyze the phase-space distribution of the 164 Sgr stream candidates. The proper motion distribution is shown in Figure 3. The colors show the $\tilde{\Lambda}_\odot$ value of each star, which helps identify the leading and trailing arms. From this figure, we can see that leading and trailing arms have different proper motion distributions and most stars have small proper motion error in both R.A. and decl. directions.

We are showing "the 3D orbit precession" in Figure 4. The *X*, *Y*, and *Z* positions with arrows representing the direction and magnitude of the V_x, V_y, and V_z velocities. We can see the Sgr stream stars as clumps on this figure. In the middle of the Figure 4, we can see the Sgr stream orbit well because the (*X,Z*) plane is mostly aligned with the orbital plane of the stream. From the orbit distribution we can see leading and trailing arms have a significant velocity segregation. In the (*X, Z*) plane, both the leading and trailing arms have opposite velocity distributions. The red small dots show stars having a $V_y > 0\,\mathrm{kms}^{-1}$, and the blue dots show stars having a $V_y < 0\,\mathrm{kms}^{-1}$. In the (*X, Y*) and (*Y, Z*) plane it is hard to see orbital direction clearly. Thanks to the *Gaia* proper motion we are capable of tracing the 3D orbit precession for the whole Sgr stream. We also illustrate the V_x, V_y, and V_z velocity distribution along the $\tilde{\Lambda}_\odot$ in Figure 5.

In Figure 6, we examine the angular momentum (*L*) versus energy (*E*) space of the Sgr stream candidates. This is the first time that this stream has been inspected using this method. From Figure 6 we can see that the leading and trailing arms have slightly different distributions in angular momentum versus energy space, but are coincident in L_x versus L_y and L_x versus L_z space. This figure makes us confident that the stars we are selecting all belong to the same substructure, and thus our Sgr selection method was good.

As noted, a velocity separation is seen for the leading and trailing arms in the (*X, Z*) plane. For the leading arm, we can see that the components of angular momentum show two distinct parts especially in the (L_x, L_z) and (L_y, L_z) planes. For the trailing arm we did not see clear component separation.

3.4. Metallicity Distribution Function of Sgr Stream

Recently, Gibbons et al. (2017) demonstrated that the Sgr stream has two subpopulations with distinct chemistry and kinematics. Using our photometric metallicity estimation relation, we are able to estimate metallicities for our Sgr stars in a large $\tilde{\Lambda}_\odot$ range. Figure 7 presents the metallicity

distribution of the leading and trailing arms in six $\tilde{\Lambda}_{\odot}$ bins (three for the leading arm and three for the trailing arm). As we can see from the left panel, the trailing arm has a broad metallicity distribution, but considering the Poisson error, it is hard to say whether there is an obvious metallicity gradient along the trailing arm. In the right panel, the leading arm stars show a slight metallicity gradient in all three $\tilde{\Lambda}_{\odot}$ bins (peak shift from upper panel to lower panel). Thus we did not see an obvious [Fe/H] gradient in either the leading and trailing arm. When comparing the [Fe/H] between leading and trailing arms, we also did not see a significant difference. This could be because our data is not complete and we still need more data to do the analysis.

4. Discussion and Conclusion

Combined with *Gaia* DR2 proper motion, we published 164 Sgr stream members in the LAMOST DR4 sample with various parameters. We showed the proper motion distribution feature for all Sgr stream members. We traced the Sgr stream in 6D phase-space across the sky coverage. We find that the leading and trailing arms have slightly different energy and total angular momentum distribution. We see that the leading arm in the (X, Z) plane has an obvious velocity segregation, which we can also see in the component of angular momentum. By comparing our Sgr stream data with various N-body models, we find that none of these models are consistent with our observation data. The new model from Dierickx & Loeb (2017) is consistent with our Sgr data in distance versus $\tilde{\Lambda}_{\odot}$ space, but the leading tail is significantly undervalued compared with observation. The L&M model provided an obviously lower estimation of the distance of the Sgr trailing tail. Also the velocity for the trailing tail does not match observations.

Our data shows that the trailing arm reaches apogalacticon at ($\tilde{\Lambda}_{\odot} \sim 170°$) with a heliocentric distance $\sim$130 kpc. The apogalacticon feature identified with the M-giant are consistent with the result of Sesar et al. (2017b) who used RR Lyrae stars to unveil similar features. In previous works, this branch was only seen in BHBs and RR Lyrae stars (Belokurov et al. 2014; Sesar et al. 2017b). Both of two stellar tracers are only found in metal-poor populations; in other words, this branch should be an earlier evolved branch, which can only be traced by a metal-poor population. However, our work detects a metal-rich population of M giants, implying that the Sgr stream may be composed of various stellar populations with a broad metallicity range. Carlin et al.'s (2018) results (and Hasselquist et al. 2017 APOGEE abundances) show that even though we know Sgr has many stellar populations (Siegel et al. 2007) and a large metallicity spread, stars from all of these populations follow similar abundance trends (e.g., as a function of [Fe/H]).

From the metallicity of Sgr stream stars, the mean value for the leading arm is -1.86 dex, the mean value for the trailing arm is -1.60 dex. The metallicity of the trailing arm is richer than that of the leading arm, and the results are consistent with previous detections (Chou et al. 2007; Li et al. 2016; Carlin et al. 2018). We see that both the leading and trailing arms have a broad metallicity distribution, which can be separated into two subpopulations, but for the inner leading and trailing arms, we did not see a significant metallicity gradient. So we speculate that, when the Sgr dwarf galaxy interacts with our MW, the stripping process occurs, removing the whole population at the same time instead of removing the halo metal-poor stars first.

The authors wish to thank Marion I.P. Dierickx and Jorge Penarrubia for sharing their model data. We thank the referee for helpful comments. This work was supported by National Natural Science Foundation of China (NSFC) under grants 11703019 and China West Normal University grants 17C053,17YC507 and 16E018. C.L. acknowledges the NSFC under grants 11373032 and 11333003. X.-X.X. is thankful for the support of Recruitment Program of Global Youth Experts of China and NSFC under grants 11390371, 11873052,11890694. J.Z. would like to acknowledge the NSFC under grants 11503066 and U1731129. J.W. thanks the NSF for their support through grant No. AST-1615688. Guoshoujing Telescope (the Large Sky Area Multi-Object Fiber Spectroscopic Telescope LAMOST) is a National Major Scientific Project built by the Chinese Academy of Sciences. Funding for the project has been provided by the National Development and Reform Commission. LAMOST is operated and managed by the National Astronomical Observatories, Chinese Academy of Sciences. The LAMOST FELLOWSHIP is supported by Special Funding for Advanced Users, budgeted and administrated by Center for Astronomical Mega-Science, Chinese Academy of Sciences (CAMS). This work has made use of data from the European Space Agency (ESA) mission *Gaia* (https://www.cosmos.esa.int/gaia), processed by the *Gaia* Data Processing and Analysis Consortium (DPAC, https://www.cosmos.esa.int/web/gaia/dpac/consortium). Funding for the DPAC has been provided by national institutions, in particular, the institutions participating in the *Gaia* Multilateral Agreement. This project was developed in part at the 2018 *Gaia*-LAMOST Sprint workshop, supported by the NSFC under grants 11333003 and 11390372.

ORCID iDs

Chao Liu https://orcid.org/0000-0002-1802-6917
Jing Zhong https://orcid.org/0000-0001-5245-0335
Jake Weiss https://orcid.org/0000-0003-2743-8937
Jeffrey L. Carlin https://orcid.org/0000-0002-3936-9628
Hao Tian https://orcid.org/0000-0003-3347-7596

References

Belokurov, V., Koposov, S. E., Evans, N. W., et al. 2014, MNRAS, 437, 116
Belokurov, V., Zucker, D. B., Evans, N. W., et al. 2006, ApJL, 642, L137
Carlin, J. L., Sheffield, A. A., Cunha, K., & Smith, V. V. 2018, ApJL, 859, L10
Chou, M.-Y., Majewski, S. R., Cunha, K., et al. 2007, ApJ, 670, 346
Cui, X.-Q., Zhao, Y.-H., Chu, Y.-Q., et al. 2012, RAA, 12, 1197
Davenport, J. R. A., Ivezić, Ž., Becker, A. C., et al. 2014, MNRAS, 440, 3430
Dehnen, W. 2000, AJ, 119, 800
Dehnen, W., & Binney, J. J. 1998, MNRAS, 298, 387
Deng, L.-C., Newberg, H. J., Liu, C., et al. 2012, RAA, 12, 735
Dierickx, M. I. P., & Loeb, A. 2017, ApJ, 836, 92
Gaia Collaboration, Brown, A. G. A., Vallenari, A., et al. 2018, A&A, 616, A1
Gibbons, S. L. J., Belokurov, V., & Evans, N. W. 2017, MNRAS, 464, 794
Gizis, J. E. 1997, AJ, 113, 806
Hasselquist, S., Shetrone, M., Smith, V., et al. 2017, ApJ, 845, 162
Holtzman, J. A., Hasselquist, S., Shetrone, M., et al. 2018, AJ, 156, 125
Ibata, R. A., Gilmore, G., & Irwin, M. J. 1994, Natur, 370, 194
Ji, W., Cui, W., Liu, C., et al. 2016, ApJS, 226, 1
Johnson, D. R. H., & Soderblom, D. R. 1987, AJ, 93, 864
Koposov, S. E., Belokurov, V., Evans, N. W., et al. 2012, ApJ, 750, 80
Koposov, S. E., Belokurov, V., Zucker, D. B., et al. 2014, MNRAS, 446, 3110
Koposov, S. E., Belokurov, V., Zucker, D. B., et al. 2015, MNRAS, 446, 3110
Law, D. R., & Majewski, S. R. 2010, ApJ, 714, 229
Lépine, S., Hilton, E. J., Mann, A. W., et al. 2013, AJ, 145, 102
Lépine, S., Rich, R. M., & Shara, M. M. 2003, AJ, 125, 1598
Lépine, S., Rich, R. M., & Shara, M. M. 2007, ApJ, 669, 1235
Li, J., Smith, M. C., Zhong, J., et al. 2016, ApJ, 823, 59

Li, Y.-B., Luo, A.-L., Du, C.-D., et al. 2018, ApJS, 234, 31
Luo, A.-L., Zhao, Y.-H., Zhao, G., et al. 2015, RAA, 15, 1095
Majewski, S. R., Skrutskie, M. F., Weinberg, M. D., & Ostheimer, J. C. 2003, ApJ, 599, 1082
Mann, A. W., Gaidos, E., Lépine, S., & Hilton, E. J. 2012, ApJ, 753, 90
Meyer, M. R., Edwards, S., Hinkle, K. H., & Strom, S. E. 1998, ApJ, 508, 397
Navarro, J. F., Frenk, C. S., & White, S. D. M. 1996, ApJ, 462, 563
Newberg, H. J., & Carlin, J. L. 2016, Tidal Streams in the Local Group and Beyond: Observations and Implications (Berlin: Springer), 420
Newberg, H. J., Yanny, B., Rockosi, C., et al. 2002, ApJ, 569, 245
Peñarrubia, J., Belokurov, V., Evans, N. W., et al. 2010, MNRAS, 408, L26
Reid, I. N., Hawley, S. L., & Gizis, J. E. 1995, AJ, 110, 1838
Schlafly, E. F., & Finkbeiner, D. P. 2011, ApJ, 737, 103
Schlegel, D. J., Finkbeiner, D. P., & Davis, M. 1998, ApJ, 500, 525
Sesar, B., Hernitschek, N., Dierickx, M. I. P., Fardal, M. A., & Rix, H.-W. 2017b, ApJL, 844, L4
Sesar, B., Hernitschek, N., Mitrović, S., et al. 2017a, AJ, 153, 204
Siegel, M. H., Dotter, A., Majewski, S. R., et al. 2007, ApJL, 667, L57
Wright, E. L., Eisenhardt, P. R. M., Mainzer, A. K., et al. 2010, AJ, 140, 1868
Zhao, G., Zhao, Y.-H., Chu, Y.-Q., et al. 2012, RAA, 12, 723
Zhong, J., Lépine, S., Li, J., et al. 2015, RAA, 15, 1154